Electronic Supplementary Information (ESI) for

Extraordinarily High Pseudocapacitance of Metal Organic Framework Derived Nanostructured Cerium Oxide

Sandipan Maiti, Atin Pramanik and Sourindra Mahanty*
Fuel Cell & Battery Division
CSIR-Central Glass & Ceramic Research Institute
Kolkata 700032 India
and CSIR-Network Institutes for Solar Energy (NISE), India

*Correspondence to be addressed to: mahanty@cgcri.res.in; s_mahanty@hotmail.com
Tel: +91-33-2322 3495 Fax: +91-33-2473 0957

Contents

1. Experimental

1.1 Synthesis of Ce(1,3,5-BTC)$(H_2O)_6$ and Ce-MOF derived CeO_2
Scheme-1: Schematic representation of the synthesis of MOF derived CeO_2
Scheme-2: Formation mechanism of Ce(1,3,5-BTC)$(H_2O)_6$ and MOF derived CeO_2
1.2 Material characterization
1.3 Electrochemical characterization
1.4 Calculation of capacitance (C), specific capacitance (Cs), energy density (E), power density (P) and coulombic efficiency (η)

2. Additional Supporting Data

Fig.S1: Structural characterization of the synthesized Ce(1,3,5-BTC)$(H_2O)_6$: (a) X-ray diffractogram of synthesized Ce(1,3,5-BTC)$(H_2O)_6$ (b) FTIR spectrum of 1,3,5-H_3BTC used as precursor (c) FTIR spectrum of synthesized Ce(1,3,5-BTC)$(H_2O)_6$

Fig.S2: TGA curves for the synthesized Ce(1,3,5-BTC)$(H_2O)_6$ MOF

Fig.S3: Morphological characterization: (a) Low magnification FESEM image of Ce(1,3,5-BTC)$(H_2O)_6$ shows the sheaf like assembly of the Ce-BTC MOF nanobars (b) Low magnification FESEM images of CeO_2 and (b) High magnification TEM image of CeO_2

Fig.S4: Raman spectrum of the MOF derived nanostructured CeO_2 in the range 200-1200 cm^{-1}

Fig.S5: (a) & (b) N_2 adsorption-desorption isotherms of synthesized Ce(1,3,5-BTC)$(H_2O)_6$ and CeO_2 respectively and (c) & (d) corresponding pore size distributions

Fig.S6: (a) Cyclic voltammetry of CeO_2 at different scanning rate in 3 M KOH+ 0.05M $K_4Fe(CN)_6$. The nature of the CV curves are found to be similar to those in 3 M KOH+ 0.1M $K_4Fe(CN)_6$ (b) Plots of specific peak current vs square root of scan rate (Randles-Sevcik plot) for MOF derived CeO_2 electrode in 3 M KOH, 3 M KOH + 0.05M $K_4Fe(CN)_6$ and 3 M KOH + 0.1 M $K_4Fe(CN)_6$

Fig.S7: Cyclic voltammograms of supercapacitor cell constructed with 3 M KOH + 0.1 M $K_4Fe(CN)_6$ as electrolyte using bare Ni foam as working electrode at different scan rates ranging from 2 mVs^{-1} to 100 mVs^{-1}

Fig.S8: Galvanostatic charge-discharge curves for CeO_2 in 3 M KOH and in 3 M KOH + 0.1 M $K_4Fe(CN)_6$ at high current densities of (a) 5 Ag^{-1} and (b) 10 Ag^{-1}.

1. Experimental:

1.1 *Synthesis of Ce(1,3,5-BTC)$(H_2O)_6$ and Ce-MOF derived CeO_2*

All chemicals were used as received without further purification. Ultrapure water was used in all experiments and was obtained from a three-stage Millipore Mill-Q (Merck, Germany) purification system.

Ce(1,3,5-BTC)$(H_2O)_6$ MOF was synthesized through a simple low temperature solvothermal method reported elsewhere.[1] In a typical synthesis, saturated aqueous solution of $Ce(NO_3)_3.6H_2O$ (4.34 g, 10 mmol) was added into a water-ethanol solution (v/v=1:1) of 1,3,5-H_3BTC (2.10 g, 10 mmol) under vigorous stirring and kept on a hot plate in a closed glass container at 60°C. A large amount of white precipitate occurred almost immediately. After continuing the process for 1 h, the precipitate was collected by centrifugation and washed several times with ethanol and water. Finally, the product, Ce(1,3,5-BTC)$(H_2O)_6$ MOF, was dried at 60°C for 12 h in an air oven.

CeO_2 was synthesized via calcination of Ce(1,3,5-BTC)$(H_2O)_6$ MOF in an air-furnace at 650°C for 3 h and a heating rate of 2°C per min. The resulting powder was straw yellow in colour.

Scheme-1: Schematic representation of the synthesis of MOF derived CeO_2.

Scheme-2: Formation mechanism of Ce(1,3,5-BTC)$(H_2O)_6$ MOF and MOF derived CeO_2

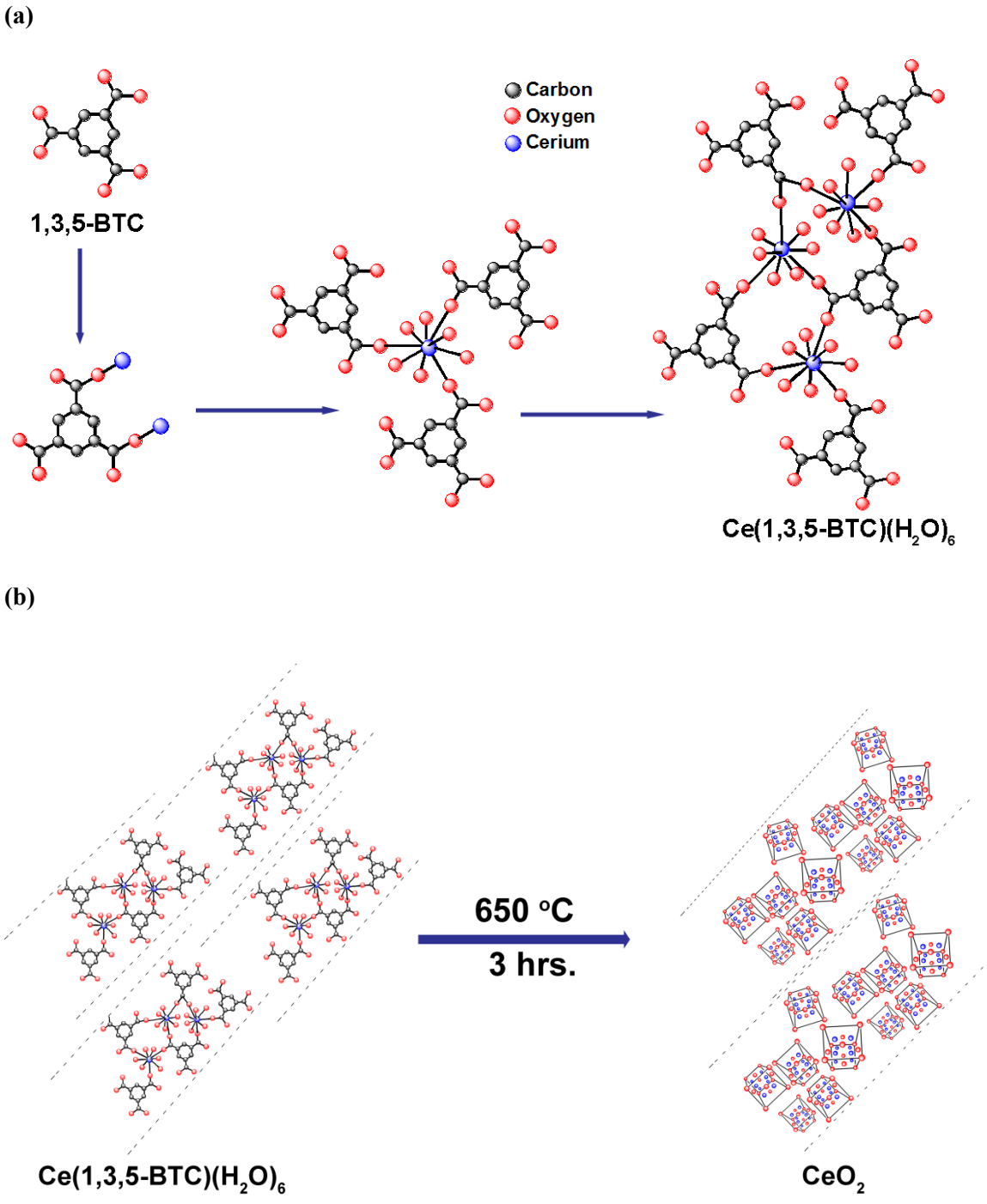

1.2 *Material characterization*

X-ray powder diffractograms were recorded in the 2θ range 5°-50° and 20°-80° at a scanning rate of 2° min^{-1} by an X-ray diffractometer (Philips X'Pert, The Netherlands) with a Cu- Ka radiation at 40 KV and 40 mA. Phase analyses of the X-ray diffraction profiles were carried out using PANalytical HighscorePlus program. Microstructure and morphology of the synthesized powder were investigated by a field emission scanning electron microscope (ZEISS Supra 35, Germany). A

transmission electron microscope (TEM), Tecnai G^2 30ST (FEI) with an accelerating voltage of 300 kV was used to obtain the high resolution TEM images (HRTEM) and selected area electron diffraction (SAED) pattern. Fourier transform infrared spectroscopy (FT-IR) was carried out to identify the characteristic bands in the wave number range from 4000 to 400 cm^{-1} using a BOMEN infrared spectrophotometer, engaging in transmission mode through KBr (spectroscopy grade) disc formation. Synthesized CeO_2 nanowires have been further characterized by a Renishaw In Via Reflex micro Raman spectrometer using 514 nm line of an Ar^+ ion laser for excitation in the range 200-2000 cm^{-1}. Thermogravimetric analysis (TGA) of the powder samples were carried out under argon flow at a heating rate of 10^{o}C min^{-1} using Simultaneous Thermal Analyzer (STA 449F, Netzsch, Germany). Nitrogen adsorption-desorption measurements were carried out using a Quantachrome Autosorb surface analyzer at 77.3 K. The sample was degassed under vacuum at 200^{o}C for 3 h prior to measurement. The specific surface area of MnO_2 was measured by nitrogen gas absorption through Brunauer-Emmett-Teller (BET) method. Pore size distribution was estimated from desorption isotherm by the Barrett-Joyner-Halenda (BJH) method. Pore volume was determined from the amount of nitrogen adsorbed at $P/P_0 = 0.98$.

1.3 *Electrochemical characterization*

The working electrodes were fabricated by mixing 80 wt% active material (MOF derived CeO_2), 15 wt% SuperP carbon and 5 wt% polytetrafluoroethylene (PTFE) in isopropyl alcohol (IPA) to form a viscous paste and casted on (2 cm x 2 cm) nickel foam (thickness ~ 0.2 mm). The electrodes were heated at 110^{o}C for 12 h in a vacuum oven to evaporate the residual solvent. The typical mass loading of CeO_2 on Ni foam was about 0.5 mg/cm^2. The accuracy of electronic balance is 0.01 mg (MS105DU, Mettler Toledo, USA). A three-electrode configuration was used to conduct the electrochemical measurements. A platinum mesh (2 cm x 2 cm) and an Ag/AgCl electrode were used as the counter and reference electrode respectively, respectively. Cyclic voltammetry (CV), Galvanostatic charge-discharge, electrochemical impedance spectroscopy (EIS) were carried out by a Galvanostat-Potentiostat (PGSTAT 300N, Autolab, the Netherlands). All the CVs were measured between 0.0 V and 0.5 V at different scan rates of 2, 5, 10, 20, 50, 75 and 100 mVs^{-1}. Galvanostatic charge-discharge measurements were carried out at current densities of 0.2, 0.5, 1, 2, 5 and 10 Ag^{-1} in the potential range 0.0 V to 0.4 V. EIS measurements were carried out in the frequency range of 0.1 Hz-100 kHz at an open circuit potential with AC amplitude of 10 mV and the obtained data were fitted to an equivalent circuit model.

1.4 *Calculation of capacitance (C), specific capacitance (C_s), energy density (E), power density (P) and coulombic efficiency (η)*

The discharge capacitance (C), specific capacitance (C_s), energy density (E), power density (P) and coulombic efficiency (η) reported in this work were calculated from the galvanostatic charge discharge curves using the relations as given in the literature for similar profiles[2-4]:

$$C = \frac{I \times \Delta t}{\Delta V} \qquad (1)$$

$$C_s = \frac{C}{m} \qquad (2)$$

$$E = \frac{C_s \times (\Delta V)^2}{2} \quad (3)$$

$$P = \frac{E}{t} = \frac{I \times \Delta V}{2} \quad (4)$$

$$\eta = \frac{\Delta t_D}{\Delta t_C} \times 100\% \quad (5)$$

Where I is constant discharge current, m is the active mass of working electrode, ΔV is the voltage range, and Δt_D, Δt_C are discharging and charging time respectively.

To calculate the theoretical capacitance, the material should be assumed to be of monolayer thickness so that the entire surface of all the molecules could be utilized. On that principle, since one mole of a substance contains Avogardo number of molecules, the theoretical capacitance can be simply calculated from the Faraday constant:

Specific Capacitance = 96485/molecular weight (for one electron transfer process).

The theoretical capacitance value for CeO_2 comes to 560.6 F g^{-1}.

2. Additional Supporting Data:

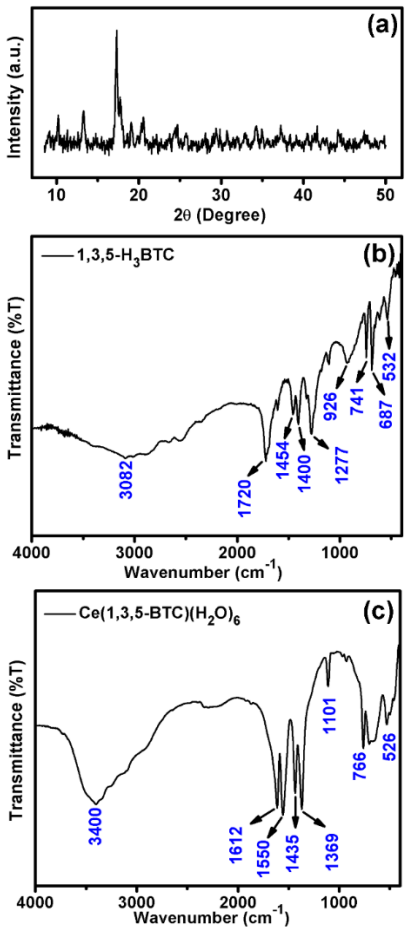

Figure S1. Structural characterization of the synthesized Ce(1,3,5-BTC)$(H_2O)_6$: (a) X-ray diffractogram of synthesized Ce(1,3,5-BTC)$(H_2O)_6$ (b) FTIR spectrum of 1,3,5-H_3BTC used as precursor (c) FTIR spectrum of synthesized Ce(1,3,5-BTC)$(H_2O)_6$.

All the observed peaks in the x-ray diffractogram are compared to the known bulk phase of La(1,3,5-BTC)$(H_2O)_6$ and Sm(1,3,5-BTC)$(H_2O)_6$.[5, 6] Absence of any additional peaks of any other phases or impurities indicate it to be a single phase material. Based on the crystal structure of the bulk La(1,3,5-BTC)$(H_2O)_6$ and Sm(1,3,5-BTC)$(H_2O)_6$,[2, 3] the crystal structure of the Ce(1,3,5-BTC)$(H_2O)_6$ is derived to be monoclinic and belong to space group Cc. FTIR data for Ce-BTC has been compared and analyzed with respect to that of 1,3,5-H_3BTC. In Ce-BTC, the central Ce atom is nine-coordinated: six oxygen atoms from water molecule and three oxygen atoms from the carboxylate groups of 1,3,5-H_3BTC ligands to generate a tricapped trigonal prismatic geometry. It is observed that in the FTIR spectrum of Ce-BTC, the characteristic bands of the non-ionized carboxyl group of 1,3,5-BTC disappear (ν_{-OH}, 3082 cm^{-1}; $\nu_{C=O}$, 1720 cm^{-1}; $\delta_{C=O}$, 532 cm^{-1}) and new bands appear in the regions 1612-1550, 1435-1369 cm^{-1}, and 526 cm^{-1} which belong to the stretching vibrations $\nu_{assy(-COO^-)}$ and $\nu_{sym(-COO^-)}$ of the carboxylate ions, and the Ce-O stretching vibration, respectively. These new bands prove that the Ce^{4+} ions have been coordinated with the 1,3,5-BTC ligands successfully. Besides, the bands $\nu_{(-OH)}$ in the FTIR spectra (Figure S1-c), which lie in the region of 3400 cm^{-1}, indicate that water molecules act as not only the solvent but also the reactant for cerium benzene-1,3,5-tricarboxylate formation.

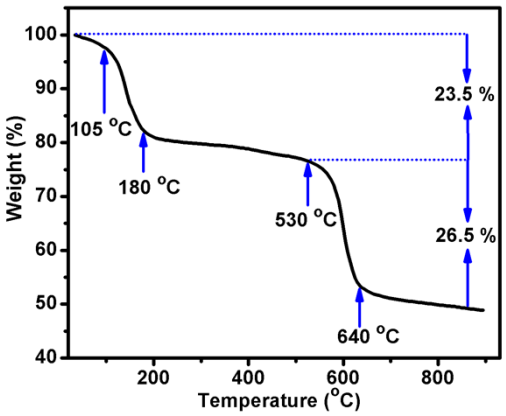

Figure S2. TGA curves for the synthesized Ce(1,3,5-BTC)$(H_2O)_6$ MOF.

Two major stages of rapid weight loss is observed in the TGA curve indicating that the Ce(1,3,5-BTC)$(H_2O)_6$ MOF decompose in two steps to produce CeO_2. The weight losses for the first and second stages were measured to be 23.5 and 26.5%, which can be assigned to loss of six water molecules (23.5%) in the first step and the organic BTC ligands (26.5 %) in the second step.

Table S1.

Structural data of the MOF derived CeO_2

Coordination of Ce 0.000000.000000.00000

Atom	Code	Distance	Error	X	Y	Z
O	1	2.340	0.0002	0.25000	0.25000	0.25000
O	193	2.340	0.0002	-0.25000	-0.25000	-0.25000
O	194	2.340	0.0002	-0.25000	-0.25000	0.25000
O	195	2.340	0.0002	-0.25000	0.25000	-0.25000
O	196	2.340	0.0002	-0.25000	0.25000	0.25000
O	197	2.340	0.0002	0.25000	-0.25000	-0.25000
O	198	2.340	0.0002	0.25000	-0.25000	0.25000
O	199	2.340	0.0002	0.25000	0.25000	-0.25000

Coordination of O 0.250000.250000.25000

Atom	Code	Distance	Error	X	Y	Z
Ce	145	2.340	0.0002	0.50000	0.50000	0.00000
Ce	97	2.340	0.0002	0.50000	0.00000	0.50000
Ce	49	2.340	0.0002	0.00000	0.50000	0.50000
Ce	1	2.340	0.0002	0.00000	0.00000	0.00000
O	7	2.702	0.0003	0.25000	0.25000	0.75000
O	4	2.702	0.0003	0.25000	0.75000	0.25000

O	2	2.702	0.0003	0.75000	0.25000	0.25000
O	196	2.702	0.0003	-0.25000	0.25000	0.25000
O	198	2.702	0.0003	0.25000	-0.25000	0.25000
O	199	2.702	0.0003	0.25000	0.25000	-0.25000

Symmetry codes:
#1 X,Y,Z; #2 -Y,X,Z; #4 Y,-X,Z; #7 X,Z,-Y; #49 X,Y+0.5000,Z+0.5000; #97 X+0.5000,Y,Z+0.5000; #145 X+0.5000,Y+0.5000,Z; #193 -Y-1,-X-1,-Z-1; #194 -X-1,-Y-1,Z; #195 -X-1,Y,-Z-1; #196 -Y-1,X,Z; #197 X,-Y-1,-Z-1; #198 Y,-X-1,Z; #199 X,Z,-Y-1;

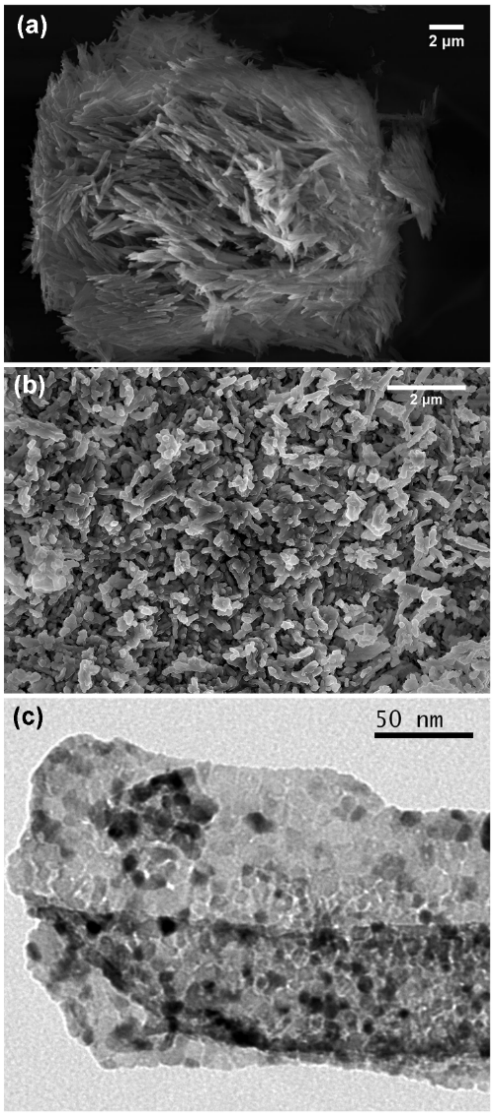

Figure S3. Morphological characterization: (a) Low magnification FESEM image of Ce(1,3,5-BTC)$(H_2O)_6$ shows the sheaf like assembly of the Ce-BTC MOF nanobars (b) Low magnification FESEM images of CeO_2 and (b) High magnification TEM image of CeO_2

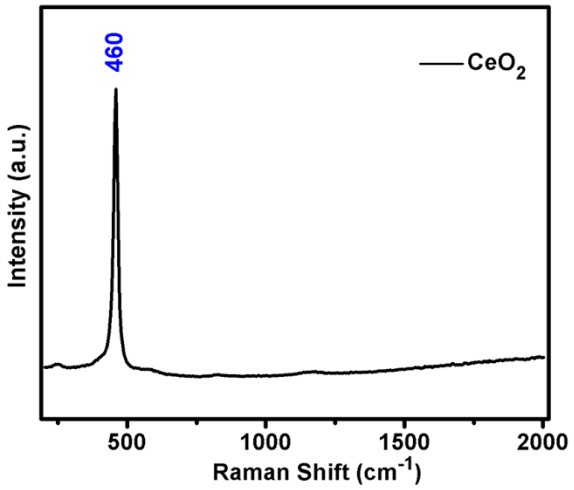

Figure S4. Raman spectrum of the MOF derived nanostructured CeO_2 in the range 200-2000 cm^{-1}. The observed sharp band at 460 cm^{-1} corresponds to F_{2g} symmetry.[7, 8]

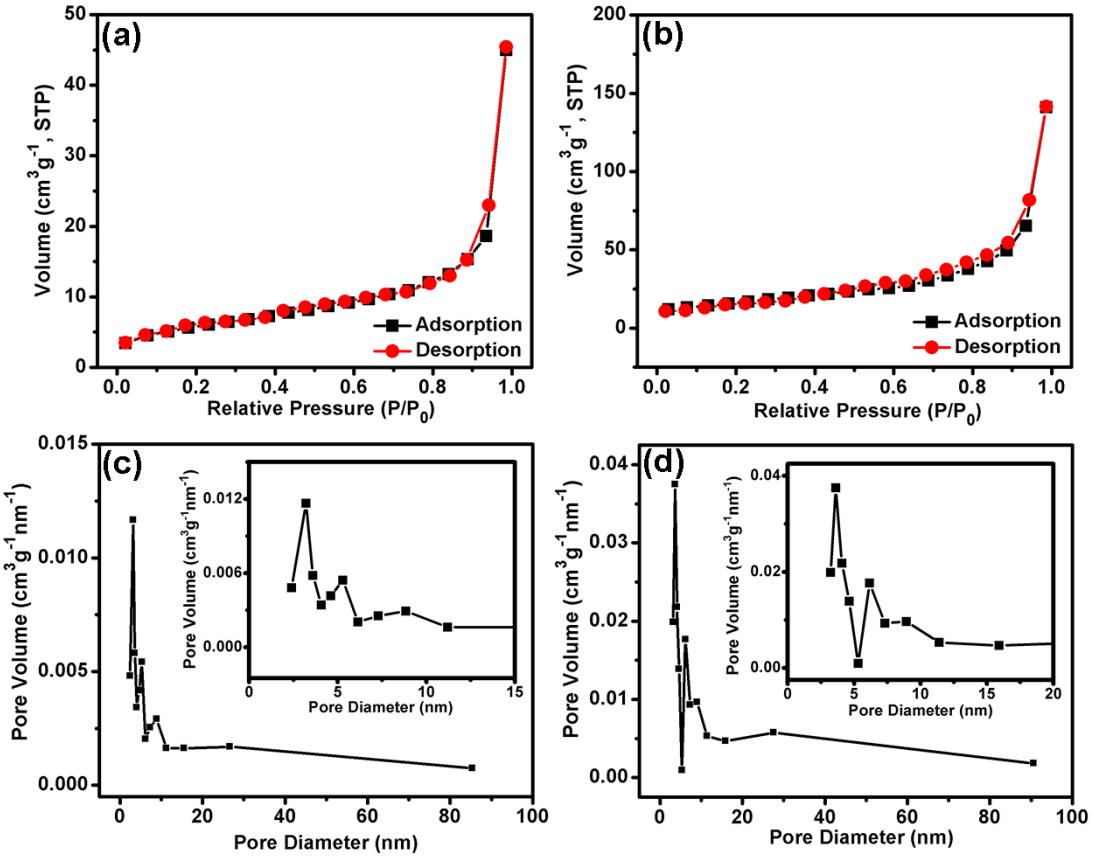

Figure S5. (a) & (b) N_2 adsorption-desorption isotherms of synthesized Ce(1,3,5-BTC)$(H_2O)_6$ and CeO_2 respectively and (c) & (d) corresponding pore size distributions. For both cases, the isotherms are convex in nature up to P/P_0 = 1.0, typical for type III isotherms; a discrete hysteresis loop starting from P/P_0 ~ 0.5 reveals a mixed H3 and H1 type indicating presence of inter-particle as well as structural pores. The corresponding pore size distributions were calculated from the adsorption part of the isotherms. Mesoporous nature with a combination of narrow and broad size distribution have been observed in both cases indicating coexistence of structural pores as well as inter-particle pores. BET surface area values are calculated to be 27.3 and 77 m^2g^{-1} respectively for Ce-BTC and CeO_2. A significant increase in the pore volume in CeO_2 compared to the parent Ce-BTC can related to presence of a large number of voids in its unique *brick-upon-tile* morphology. The total pore volume of CeO_2 is found to be 0.217 cm^3g^{-1}. Considering that the Born radius of $Fe(CN)_6^{4-}/Fe(CN)_6^{3-}$ being ~0.4 nm[9,10], a large number of the redox additive anions could be accommodated.

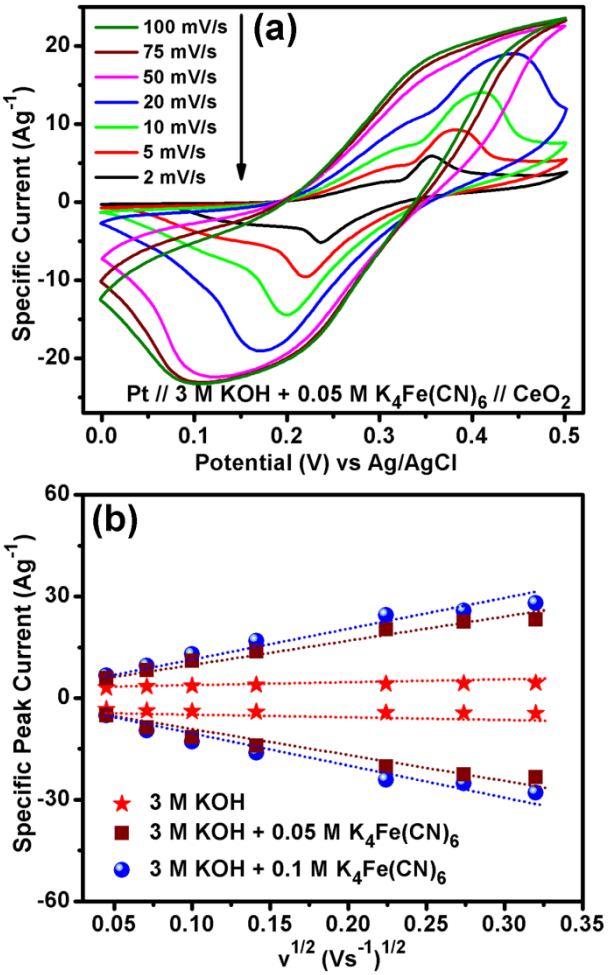

Figure S6. (a) Cyclic voltammetry of CeO_2 at different scanning rate in 3 M KOH+ 0.05M $K_4Fe(CN)_6$. The nature of the CV curves are found to be similar to those in 3 M KOH+ 0.1M $K_4Fe(CN)_6$ (b) Plots of specific peak current vs square root of scan rate (Randles-Sevcik plots) for MOF derived CeO_2 electrode

in 3 M KOH, 3 M KOH + 0.05M $K_4Fe(CN)_6$ and 3 M KOH + 0.1 M $K_4Fe(CN)_6$. A near-linear increase in peak current with increasing scan rate is indicative of diffusion controlled redox processes.

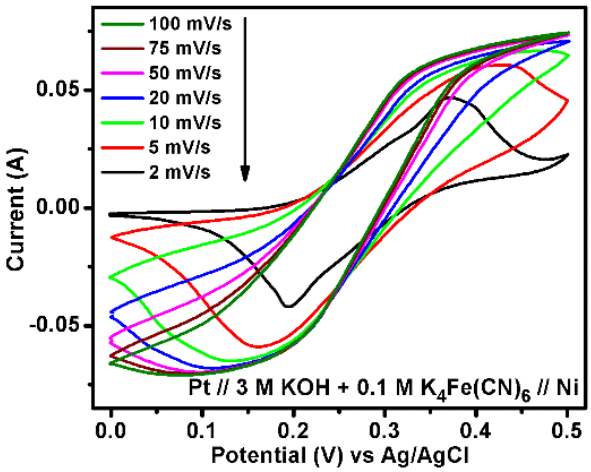

Figure S7. Cyclic voltammograms of supercapacitor cell constructed with 3 M KOH + 0.1 M $K_4Fe(CN)_6$ as electrolyte using bare Ni foam as working electrode at different scan rates ranging from 2 mVs^{-1} to 100 mVs^{-1}. A pair of redox peaks is observed at $Fe(CN)_6^{4-}/Fe(CN)_6^{3-}$ couple at 020/0.37 V. These values being very close to the observed redox potentials of Ce^{IV}/Ce^{III} (0.23/0.35) would supplement the redox reactions at the electrode/electrolyte interface by acting as an electron buffer source.[11-13] Further, conjugation of electrochemically reversible $Fe(CN)_6^{4-}/Fe(CN)_6^{3-}$ couple to quasi-reversible Ce^{IV}/Ce^{III} would reduce the ionic diffusion resistance enhancing the redox kinetics.

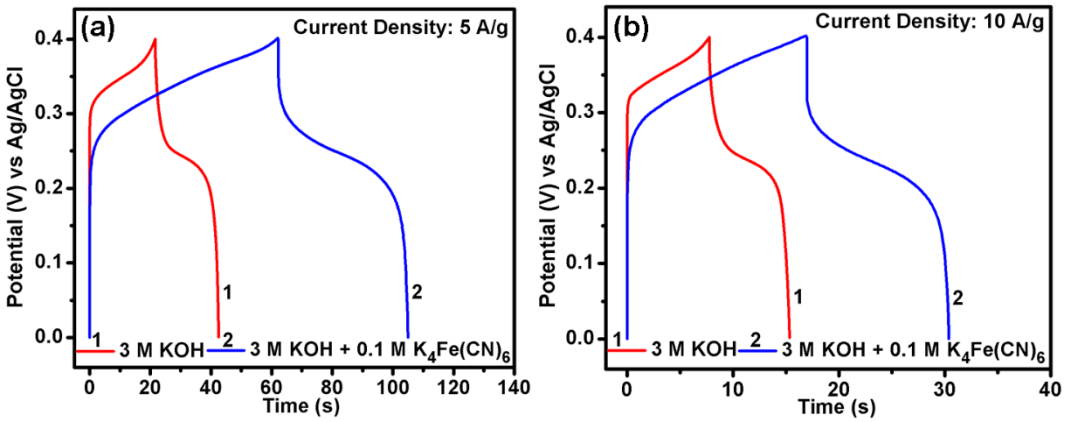

Figure S8. Galvanostatic charge-discharge curves for CeO_2 in 3 M KOH and in 3 M KOH + 0.1 M $K_4Fe(CN)_6$ at high current densities of (a) 5 Ag^{-1} and (b) 10 Ag^{-1}. The obtained specific capacitance values are 272 and 603 Fg^{-1} at 5 Ag^{-1} and 206 and 435 Fg^{-1} at 10 Ag^{-1} in 3 M KOH and in 3 M KOH + 0.1 M $K_4Fe(CN)_6$ respectively demonstrating the positive effect of redox additive.

References:

1 K. Liu, H. You, G. Jia, Y. Zheng, Y. Huang, Y. Song, M. Yang, L. Zhang and H. Zhang, *Cryst. Growth Des.*, 2010, **10**, 790-797.

2 H. B. Li, M. H. Yu, F. X. Wang, P. Liu, Y. Liang, J. Xiao, C. X. Wang, Y. X. Tong and G. W. Yang, *Nat. Commun.,* 2013, **4**, 1894-1900.
3 A. Pendashteh, M. S. Rahmanifar, R. B. Kanerc and M. F. Mousavi, *Chem. Commun.,* 2014, **50**, 1972-1975
4 H. Wang, H. S. Casalongue, Y. Liang, and H. Dai, *J. Am. Chem. Soc.,* 2010, **132**, 7472-7477.
5 Y. H. Wen, J. K. Cheng, Y. L. Feng, J. Zhang, Z. J. Li and Y. G. Yao, *Chin. J. Struct. Chem.*, 2005, **24**, 1440.
6 C. Daiguebonne, Y. Gerault, F. LeDret, O. Guillou and K. J. Boubekeur, *J. Alloys Compd.*, 2002, **344**, 179-185.
7 P. Fornasiero, G. Balducci, R. Di Monte, J. Kaspar, V. Sergo, G. Gubitosa, A. Ferrero and M. Graziani, *J. Catal.*, 1995, **164**, 173-183.
8 B. Tatar, E. D. Sam, K. Kutlu and M. Urgen, *J. Mater. Sci.*, 2008, **43**, 5102-5108.
9 G. A. Tsirlina, N. V. Titova, R. R. Nazmutdinov and O. A. Petrii, *Rus. J. Electrochem.,* 2001, **37**, 15-25.
10 A.D. Becke, *J. Chem. Phys.,* 1993, **98**, 1372-77
11 S. Maiti, A. Pramanik and S. Mahanty, *ACS Appl. Mater. Interfaces*, 2014, **6**, 10754-10762.
12 L. H. Su, X. G. Zhang, C. H. Mi, B. Gao and Y. Liu, *Phys. Chem. Chem. Phys.*, 2009, **11**, 2195-2202;
13 C. Zhao, W. Zheng, X. Wang, H. Zhang, X. Cui and H. Wang, *Sci. Rep.*, 2013**, 3**, 2986.